A 25 Mbps, 12.4 pJ/bit DQPSK Backscatter Data Uplink for the NeuroDisc Brain Computer Interface

James Rosenthal, *Student Member, IEEE,* †Apoorva Sharma, *Student Member, IEEE,*
†Eleftherios Kampianakis, *Student Member, IEEE,* and Matthew S. Reynolds, *Senior Member, IEEE*

Abstract—**Wireless brain-computer interfaces (BCIs) are used to study neural activity in freely moving non-human primates (NHPs). However, the high energy consumption of conventional active radios is proving to be an obstacle as research drives for wireless BCIs that can provide continuous high-rate data uplinks for longer durations (i.e. multiple days). We present a differential quadrature phase shift keying (DQPSK) backscatter uplink for the NeuroDisc BCI as an alternative to active radios. The uplink achieves a 25 Mbps throughput while operating in the 915 MHz industrial, scientific, and medical (ISM) band. The DQPSK backscatter modulator was measured to have an error-vector magnitude (EVM) of 9.7% and a measured power consumption of 309 μW during continuous, full-rate transmissions, yielding an analog communication efficiency of 12.4 pJ/bit.**

The NeuroDisc is capable of recording 16 channels of neural data with 16-bit resolution at up to 20 kSps per channel with a measured input-referred noise of 2.35 μV. In previous work, we demonstrated the DQPSK backscatter uplink, but bandwidth constraints in the signal chain limited the uplink rate 6.25 Mbps and the neural sampling rate to 5 kSps. This work provides new innovations to increase the bandwidth of the system, including an ultra-high frequency (UHF) antenna design with a -10 dB return loss bandwidth of 12.5 MHz and a full-duplex receiver with an average self-jammer cancellation of 89 dB. We present end-to-end characterization of the NeuroDisc and validate the backscatter uplink using pre-recorded neural data as well as *in vivo* recordings from a pigtail macaque.

Index Terms—**brain computer interfaces, biomedical devices, neural recording, backscatter communication, full-duplex radios**

I. INTRODUCTION

O VER the past few decades, electrophysiological recordings in non-human primates (NHPs) have improved our understanding of the relationship between cortical neuron dynamics and higher-level behaviors like movement and learning [1]–[3]. These advancements have generated new multidisciplinary research in the development of brain-computer interface (BCI) systems for neuroscience research and clinical medicine [4], [5].

Often these electrophysiological experiments are performed in tethered setups where an implanted micro-electrode array
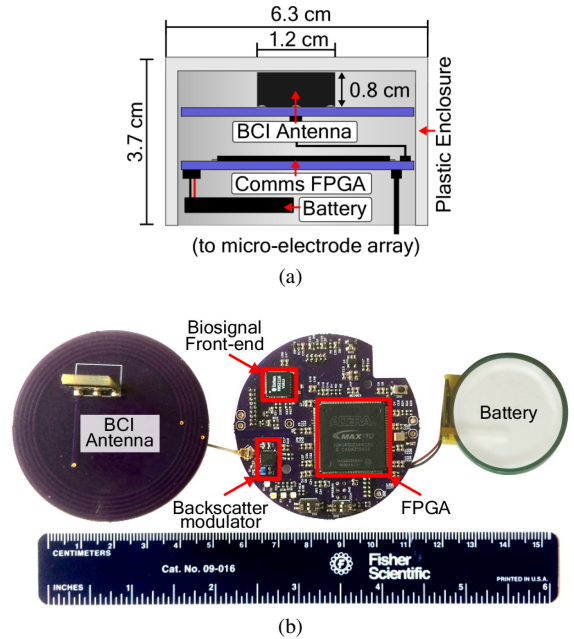
Fig. 1. (a) Drawing of the NeuroDisc in its plastic enclosure and (b) photo of the three main components that comprise the NeuroDisc: the BCI antenna, the Comms FPGA, and the battery

(MEA) connects to rack-mounted measurement equipment with cables. Such experimental setups facilitate the delivery of power and extraction of high bandwidth data from the MEAs at the cost of physically constrained test setups, reduced experimental times, and unnatural correlations in the measurement data [6].

Neuroscience research has driven development of wireless BCIs in order to record neural data from untethered, freely behaving NHPs for long durations. Ideally experiments could last uninterrupted for multiple days in order to understand both short- and long-term dynamics of cortical neural populations [3], [7]. Without external cables to transfer power and data though, these devices face severe engineering constraints in size, weight, and power consumption, limiting the battery life of most wireless BCIs to less than <48 hours [8], [9].

A major cause of the short battery life is the high energy consumption of their wireless uplink electronics [10]. Wireless BCIs often use commercially-available transmitters such as Bluetooth Low Energy [9], [11], [12] and WiFi (IEEE 802.11n) [13]. While these technologies provide reliable uplinks, they were not designed for the highly constrained energy budget of continuous neural recording applications.

Backscatter communication is an alternative method for uplinking digitized neural data at high rates and with improved energy efficiency compared to existing semi-custom radios [9],
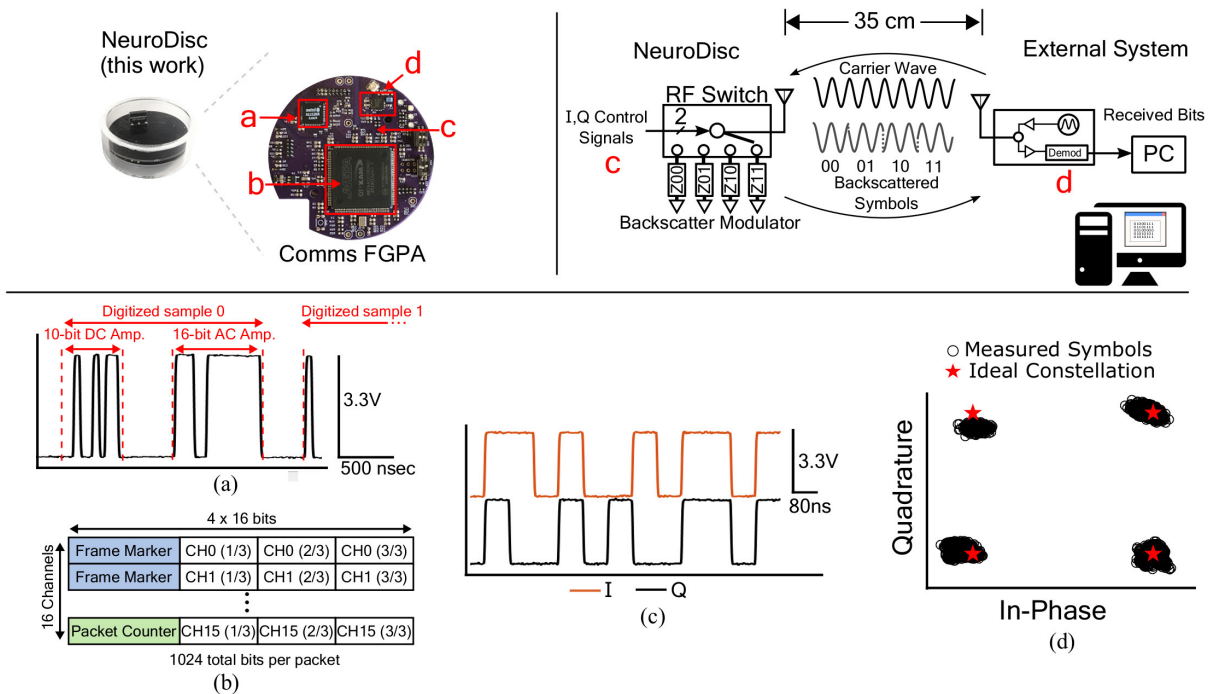
Fig. 2. An overview of the signal chain for NeuroDisc's 25 Mbps backscatter uplink. (a) Digital samples are collected by the FPGA over a serial-peripheral interface (SPI) bus. (b) Samples are assembled in a 1,024-bit packet after application of the error correction code. A packet counter is added to detect dropped packets. (c) The packet is encoded into DQPSK symbols and output from two GPIO pins on the FGPA. These signals control the backscatter modulator, determining to which impedance the BCI antenna is connected. (d) The DQPSK constellation can be measured at the receiver and decoded into symbols.

[13]. In BCI uplink architectures using active radios, the energy constrained BCI will consume a disproportionately high amount of power generating a carrier frequency and amplifying the RF signal. In backscatter uplink architectures, an external system with a rich energy source, e.g. mains power, broadcasts a single-tone RF carrier wave (CW), and the backscatter modulator on the BCI can then encode digital symbols on the incident CW by switching the impedance of its antenna and reflecting the modulated CW back to the receiver [14]. This backscatter modulation process can be performed by an RF switch [15], significantly reducing energy consumption at the BCI. The drawback to backscatter communication is a less favorable link budget, because of round-trip path losses for the CW [16]. However, in a controlled environment like an animal's home cage, a link budget can be designed to achieve reliable communication [17].

The NeuroDisc presented here (Fig. 1) uses a backscatter uplink leveraging differential quadrature phase shift keying (DQPSK) to achieve a spectral efficiency of two bits per symbol, yielding a data rate of 25 Mbps. Previous BCIs using backscatter communication have used amplitude shift keying (ASK) [18] at 1 Mbps and binary phase shift keying (BPSK) at 5 Mbps [15] which transmit data with a spectral efficiency of one bit per symbol. While backscatter modulators have been demonstrated using 16 state quadrature amplitude modulation (16-QAM) [19], and a 32-QAM backscatter integrated circuit with a 2.5 Mbps data throughput and 45.2 pJ/bit energy efficiency was presented in [20], neither of those modulators were validated in a complete system. The NeuroDisc's all-digital backscatter modulator consumes only 309 µW and

has an energy efficiency of 12.4 pJ/bit at a throughput of 25 Mbps, which is orders of magnitude lower energy per bit than commercially available transmitters.

This work is an extension of a previous 6.25 Mbps DQPSK backscatter uplink that we presented in [21]. We have previously validated the link budget and provided *in vitro* electromagnetic simulations and measurements of the 6.25 Mbps system within a metal NHP cage in [17]. In this paper we present new innovations that expand the bandwidth of the complete RF signal chain to enable an energy efficient 25 Mbps DQPSK backscatter uplink. Section II provides an overview of the NeuroDisc system design, including the BCI antenna, the Comms FPGA, the DQPSK backscatter modulator, and the custom full-duplex receiver. Section III presents our experimental results with the NeuroDisc that include a characterization of the 25 Mbps DQPSK backscatter uplink, a comparison of the NeuroDisc to an existing neural recording system [22], and 16-channels of *in vivo* recordings from a pigtail macaque. Section IV concludes with a discussion of the results, conclusions, and future work.

II. NEURODISC SYSTEM DESIGN

The NeuroDisc is a wireless brain-computer interface (BCI) designed for neural recording experiments on NHPs. What differentiates the NeuroDisc from other wireless BCIs is its 25 Mbps DQPSK backscatter uplink. The NeuroDisc is comprised of a wide-band BCI Antenna, a Comms FPGA circuit board for command and data handling functions, and a single-cell 3.7V, 500 mAh lithium-ion battery to power the device. The total power consumption of the NeuroDisc is 160 mW,
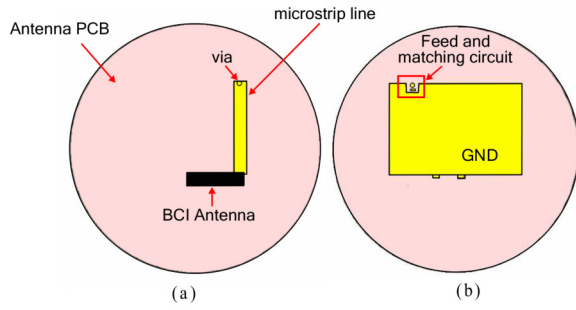
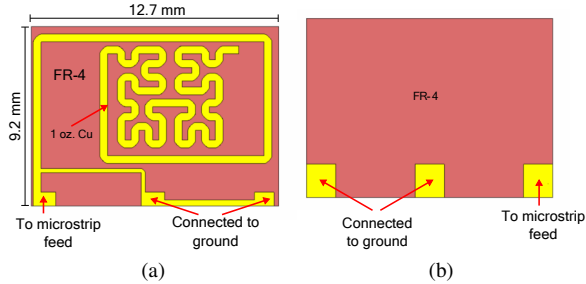Fig. 3. Layout of the antenna. (a) Top view (b) Bottom view

Fig. 4. Schematic diagram of the commercial off-the-shelf antenna element (BCI antenna). (a) Front View (b) Back View
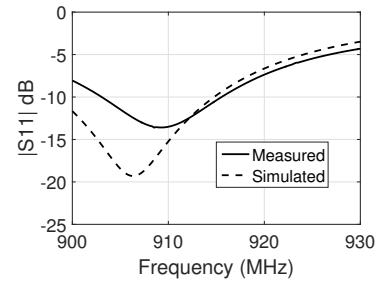

Fig. 5. (a) $|S_{11}|$ of the antenna matched well between the measured antenna and simulations. The antenna exhibited a measured -10 dB bandwidth of 12.5 MHz with a center frequency of 909 MHz.
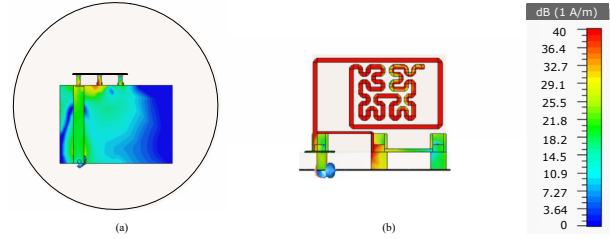

Fig. 6. Simulated surface currents on the antenna. (a) Top view showing the microstrip line (top layer) and GND plane (bottom layer) (b) Side view of the antenna element

however, only 309 μW are used for wireless communication. Nearly 90% of the total power consumption is due to the static power consumption of the particular FPGA , which was chosen to ease development of the backscatter uplink. This power draw could be significantly reduced by changing the FPGA to another device (such as the very low power Igloo Nano series from Microsemi), lowering the supply voltage, and by porting the digital design to an integrated circuit solution.

The NeuroDisc provides a low-power electrophysiology interface that can sample 16 channels at 20 kSps with 16-bit resolution, thus enabling recording of broadband neural signals. Data is then uplinked to a custom full-duplex UHF backscatter receiver that provides an external carrier wave as well as complete receiver chain that receives, demodulates, decodes, and reconstructs recordings. An overview of the NeuroDisc signal chain is shown in Fig. 2.

A. BCI Antenna Design

The NeuroDisc uses the semi-custom BCI Antenna shown in Fig. 1 and 3 for data uplink to the external system in the 915 MHz industrial, scientific, and medical (ISM) band. In previous work [21], the NeuroDisc's maximum wireless data rate was restricted to 6.25 Mbps due to a -10 dB antenna return-loss bandwidth of 1 MHz. The BCI antenna presented in this work was designed to have a wider bandwidth of 12.5 MHz to support higher data rates. It incorporates a Linx Technologies (Merlin, OR) Ant-916-USP antenna element (Fig. 3) on a custom two-layer printed circuit board (PCB) with a 55 mm outer diameter using a 1.6 mm-thick FR–4 substrate with 30 μm thick copper. This specific antenna element was chosen for this application due to its low cost, compact form factor of 12.7 mm x 9.2 mm x 2.8 mm (width

x length x height) and its wide bandwidth. As shown in Fig. 4 the antenna element is fed on the top side of the PCB with three connection pads, where one pad is connected to a 50 Ω microstrip feed line and the other two connect to a 30 mm x 20 mm rectangular ground plane on the bottom of the PCB. Included on the bottom of the PCB are a UMC coaxial connector and a passive UHF matching network consisting of a series 8.2 nH inductor and a shunt 0.3 pF capacitor.

The return-loss ($|S_{11}|$ dB) of the BCI antenna was simulated in CST Microwave Studio [23] and measured on an Agilent Technologies N5222A network analyzer to determine the antenna's bandwidth. The simulated and measured results are plotted in Fig. 5 and show comparable -10 dB return-loss bandwidths, with the simulation being between 898.2 MHz to 914.7 MHz (16.5 MHz) and the measured being between 903 to 915.5 MHz (12.5 MHz). The gain pattern and surface currents were also simulated, showing a realized gain of -13.6 dBi and surface currents concentrated on the BCI antenna (Fig. 6).

B. Comms FPGA Design

The Comms FPGA board provides command and data handling functionality to the NeuroDisc. It can be split into three main subsytems on the board: a biosignal front-end, an FPGA, and a backscatter modulator (Fig. 1). Analog signals are measured at the biosignal amplifier and digitized. The samples are then passed over a digital serial-peripheral interface (SPI) bus to the FPGA, where they are then processed, packetized, and encoded into control signals for the backscatter modulator. An overview of the signal chain is presented in Fig 2.

The biosignal front-end leverages an Intan Technologies [24] RHS2116 integrated circuit (IC). The IC provides 16 independent amplifier channels and an on-chip 16-bit analog-
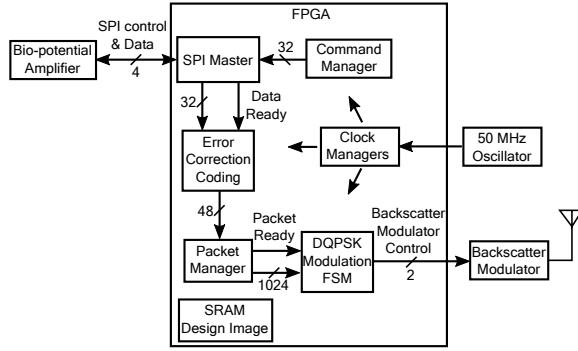
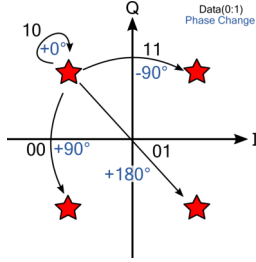Fig. 7. Block diagram of the digital logic on the FPGA

Fig. 8. State diagram depicting how data bits are mapped to DQPSK symbols. DQPSK symbols are encoded in the transitions between constellation points rather the absolute phase of constellation points.

to-digital converter (ADC) to sample each channel in a round-robin fashion at up to 20 kSps. The IC is controlled via a 32-bit SPI bus with a 12.5 MHz clock frequency.

The NeuroDisc's digital logic was implemented in Verilog on an Intel MAX10 FPGA [25] running from a 50 MHz clock. The main logic modules are shown in Fig. 7 and consist of an SPI Master, Error Correction Coding (ECC), a Packet Manager, and a DQPSK Encoder implemented as a finite state machine (FSM). The SPI Master provides a full-duplex interface for commanding the biosignal front-end and receiving digitized samples. Each sample is 32 bits long, containing 16 bits from the high-gain AC amplifier, 10-bits from the low-gain DC amplifier, and five '0' bits for padding (Fig. 2(a)). This sample is passed to the ECC module where a Hamming(16,11) ECC is applied. The benefit of using this ECC block is that it provides single error correction and dual error detection at the receiver, allowing for correction of many random independent bit errors that might occur [26]. After application of the ECC, data is passed to the Packet Manager module where the first 15 channels are concatenated with a 16-bit frame marker and the last channel is concatenated with a 16-bit packet counter in order to detect dropped packets. This process forms the 1,024-bit packet shown in Fig. 2(b). Once the packet has been generated, it is encoded as DQPSK symbols in the DQPSK Modulator FSM module.

C. DQPSK Backscatter Modulator Design

The NeuroDisc uses DQPSK backscatter modulation to uplink data to the external system. DQPSK backscatter modulation requires four unique reflection states which can be visualized as four symbols in the complex plane with equal amplitudes and offset in phase by 90°, as shown in Fig 8.

TABLE I
DQPSK MODULATOR IMPEDANCES (ADAPTED FROM [21])

| | Ideal Impedance States | | Actual Impedance States |
Z	L/C Value	ρ	L/C
Z_{00}	1.74 pF	0.5 - j0.5	1.5 pF
Z_{01}	17.39 nH	0.5 + j0.5	20 nH
Z_{10}	8.7 pF	-0.5 - j0.5	8.4 pF
Z_{11}	3.48 nH	-0.5 + j0.5	3.3 nH

In contrast to QPSK modulation which encodes data in the absolute phase of the symbol, DQPSK modulation encodes data in the phase transitions between constellation points. For example, if one begins in the top left corner of the constellation of Fig. 8 and wishes to transmit the data sequence '00', DQPSK modulation says they must move +90° to the next constellation point in the bottom left corner; if the next data sequence to transmit were '01', they would then transition +180° to the top right of the constellation, etc.

DQPSK modulation can be implemented for backscatter communication by designing a set of reflection coefficients for the antenna whose amplitude and phase match the desired constellation. Several methodologies have been investigated for altering an antenna's impedance for backscatter modulation, including the use of RF switches [27], transistors as switches [11], [28] or variable impedances [29], and digital I/O pins switching between their input and output states [30]. This work uses the switched impedance methodology of [27], which showed how arbitrary M-ary QAM backscatter constellations could be designed using RF switches with discrete impedances.

Since DQPSK requires four constellation points, four load impedances, $Z_1...Z_4$, are needed to represent them. These load impedances can be determined by specifying the desired complex power wave reflection coefficients [31], $\rho_1...\rho_4$, for each modulation state where

$$\rho_i = \frac{Z_i - Z_a^*}{Z_i + Z_a} \tag{1}$$

and Z_i represents the ith load impedance, Z_a is the input impedance of the antenna and $(\cdot)^*$ is the complex-conjugate operator.

We start by specifying the i-th ideal modulation state in the constellation by its in-phase and quadrature components, (I_i, Q_i), where $\sqrt{|I_i|^2 + |Q_i|^2} \leq 1$ since passive load impedances are used. The complex reflection coefficients are:

$$\rho_i = I_i + jQ_i, \tag{2}$$

which can be used with (1) to calculate the load impedances.

The ideal impedance values were calculated as shown in Fig. 9 and Table I. Actual impedance values differ due to component variations, parasitic impedances, and impedance mismatches on the printed circuit board and the antenna. For backscatter constellations, the worst-case differential radar cross section (RCS) [32] will determine the minimum received power and thus the bit error rate (BER). The differential RCS, $\Delta\sigma$, can be expressed as

$$\Delta\sigma = \frac{\lambda^2 G_{ND}^2}{4\pi} \min_{i,j \text{ for } i \neq j} |\rho_i^* - \rho_j^*|^2, \tag{3}$$
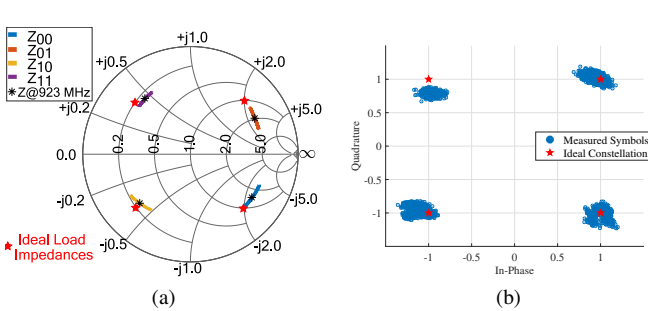
Fig. 9. (a) Impedance measurements of the DQPSK backscatter modulator states across the 900 MHz ISM band (b) Recorded symbol constellation over 5,000 symbol periods with a calculated EVM of 9.69% (adapted from [21])

where λ is the wavelength, G_{ND} is the gain of the NeuroDisc's antenna, and i and j are the i-th and j-th modulation states. As higher-order constellations such as 8-PSK or 16-QAM are used, the relative distance between constellation points is reduced, resulting in a higher BER relative to DQPSK for a given power level.

The backscatter modulator for this work uses an Analog Devices ADG904 SP4T RF switch to connect the antenna to the impedances found in the previous step. Data is encoded as DQPSK symbols in the DQPSK Modulator FSM module on the FPGA (Fig. 7). These symbols are then output from the FPGA as two parallel digital signals that control the state of the RF switch, and thus control the reflection coefficient of the BCI Antenna. As shown in Fig. 2(c) one control signal corresponds to the I component and the other to the Q component. Since the I and Q control signals are digital, they can actuate the RF switch into the four desired states. The energy consumption per bit of transmitted data was measured for the ADG904 RF switch. The switch was supplied with +3.3 V by a Keithley source-meter, and an Agilent 33500B Waveform Generator drove both control inputs of the switch at a symbol frequency of 12.5 MHz, yielding a bit rate of 25 Mbps. The total static and dynamic current of the RF switch was 93.6 µA at 3.3 V, yielding a power consumption of 309 µW.

D. Full-duplex Receiver Design

The backscattered DQPSK signals are demodulated using a semi-custom receiver design shown in Fig. 10. The receiver presented here is a modification of a previous design developed in [17] to accommodate the higher data-rate requirements. We utilize the USRP B210, a low cost commercial off-the-shelf software defined radio (SDR) to transmit the CW signal at 909 MHz and to convert the backscattered RF signals that are modulated at 25 Mbps to I/Q base band signals by processing an instantaneous bandwidth of 40 MHz. The sampled I/Q symbols are sent via a USB3 bus to an Intel Core i7 PC having a 3.8 GHz clock rate and 16 GB of memory.

One of the challenges of this work was addressing the data rate requirement for the signal processing in the receiver pipeline. In particular, the USRP samples 2x16-bit symbols (I and Q) with a rate of 40 MHz, resulting in a data-rate of 160 MBytes/sec. To address such high data-rate requirements, each component of the receiver pipeline depicted in Fig. 11
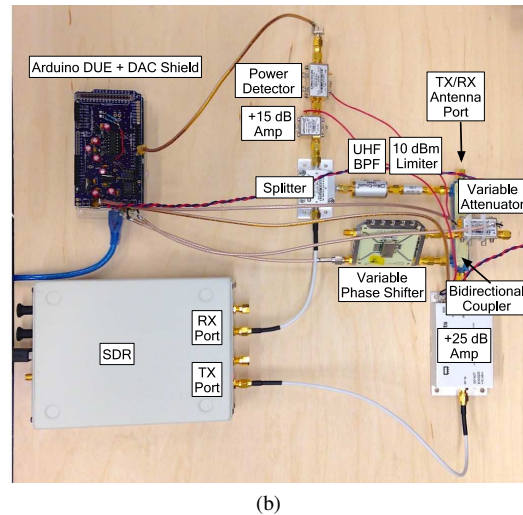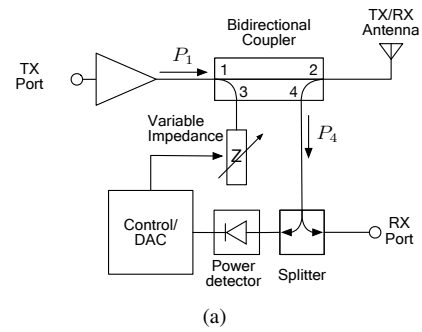

(a)

(b)

Fig. 10. (a) Block diagram of the RF interface and isolation circuitry. (b) Photo of the full-duplex DQPSK backscatter receiver, RF interface, and isolation circuitry
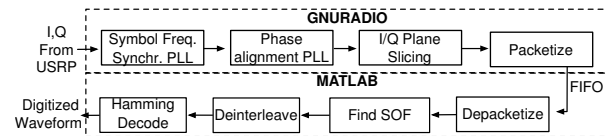

Fig. 11. Block diagram of the software flow in GNURADIO and Matlab

was carefully selected and tuned so that few to no packets would be dropped due to processing limitations. The pipeline consists of a GNURadio flowgraph that runs in realtime and implements symbol frequency synchronization and phase alignment by using carefully tuned PLLs. The resulting data stream is sliced, hard-decoded, packetized as a stream of two DQPSK symbols per byte, and then stored to disk. In turn, a custom MATLAB script processes the offline data by implementing depacketization, start-of-frame synchronization (SOF), deinterleaving and Hamming decoding to extract the digitized neural data.

A widely known idiosyncrasy of backscatter communication systems is that the relatively weak backscatter signals are demodulated in the presence of a much stronger CW signal (i.e. a self-jammer) [33]. This problem is worse in monostatic systems, where the imperfect transmit-to-receive path isolation amplifies the self-jammer, thus imposing high dynamic range requirements on the receiver [34]. As an example, for an input power of -10 dBm the maximum RX gain on the USRP that can be used without exceeding the receiver's 1-
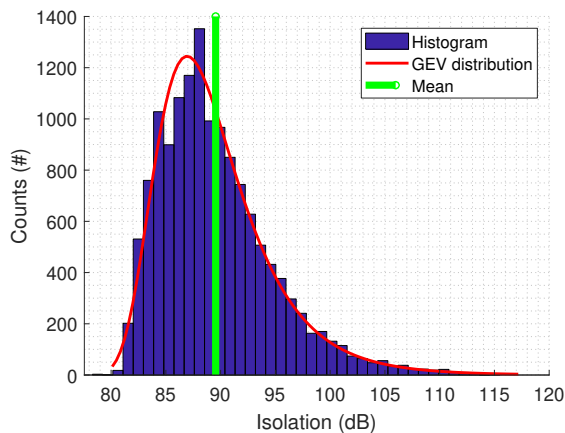
Fig. 12. Measured histogram of the self-jammer canceler's isolation performance. The data fit a generalized extreme value (GEV) distribution with a mean of 89 dB.
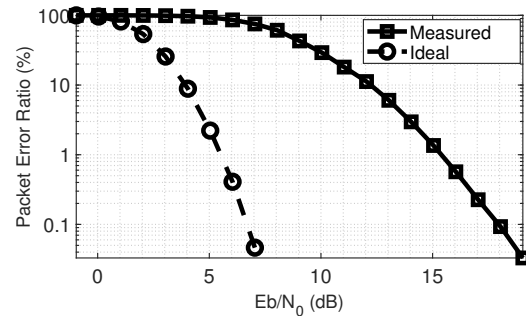

Fig. 13. Plot of the ideal and measured packet error ratio (PER) curves. Non-idealities in the receiver, such as carrier leakage, contribute to the observed difference in measured PER.

dB compression point is limited to only 20 dB out of the maximum 76 dB. Moreover, the noise figure of the USRP at such low RX gains is on the order of 30 dB; 25 dB higher than the NF exhibited in RX gains higher than 60 dB [35]. As this example demonstrates, a self-jammer cancellation system can improve the performance of the receiver by several orders of magnitude.

A full-duplex isolation circuit was developed for this work, as depicted in Fig. 10. Isolation is implemented by matching the reflection coefficient on the input-coupled port of the coupler to the reflection coefficient of the antenna. Thus, some of the input carrier wave is coupled and destructively added to the output-coupled port in order to cancel the leaked carrier [34]. By connecting variable impedance components to the input-coupled port, we can change the load's reflection coefficient. The variable impedance in this work is implemented with voltage-controlled RF phase shifter in series with a voltage-controlled RF attenuator, both from Mini-Circuits, Inc.

To find the optimal impedance, an Arduino DUE is used in combination with a power detector that is connected to the output coupled port. The Arduino finds the impedance that minimizes the measured input power from the power detector using a full-search algorithm and controls the variable impedances using two 12-bit digital-to-analog converters (DAC). A picture of the complete setup is shown Fig. 10(b)-bottom where all the components of the system can be observed, including amplifiers for the carrier wave and the RX signal, UHF bandpass filters to reject out of band interference and a 10 dBm RF limiter to protect the USRP.

III. EXPERIMENTAL RESULTS

A. Self-jammer Canceller Characterization

To evaluate the performance of the self-jammer canceller we set up the following experiment: a 50 Ω load was connected the output of a coupler and a +15 dBm CW at 909 MHz was connected to the input. Then, we tuned the variable impedance load and measured the leaked CW power at the output-coupled port using a signal analyzer. Finally, we measured the resulting isolation, defined as the ratio of transmitted to received power, after 14000 repeated tuning operations over

four hours. The results were then plotted in the histogram of Fig. 12. The variability of the isolation results suggest that *isolation can be viewed as a random variable* dependent on small impedance variations due to environmental changes, i.e. temperature fluctuations, as well as noise in the self-jammer control signals and on the power detector. In this case isolation is on the order 80-115 dB (a range of 35 dB) with a mean of 89 dB. Using MATLAB's fitting toolbox we determined that the data fits a generalized extreme value (GEV) distribution. We believe this finding is critical for the corresponding literature (e.g. [34]) because it suggests that the characterization of self-jammer cancellers include statistical properties of the system, not simply a "one-shot" measurement. To the best of our knowledge, this is a first-of-a-kind approach for the characterization of such systems.

Finally, it is important to note that the measured *mean* isolation is higher than similar systems in the literature [34]. We postulate that such high performance is due to the high control resolution of the variable impedance load. In particular, using simulations we determined that for every control resolution bit there's a 3 dB gain in the worst-case-scenario and mean isolation performance. Moreover, simulation results indicate that in our case, with a 12-bit control resolution, a mean isolation of 90 dB is to be expected. Good agreement is observed between the simulations and the measurements.

B. Packet Error Rate (PER) characterization

The reliability of the backscatter uplink was analyzed by comparing the ideal packet error ratio (PER) of a DQPSK receiver as a function of energy-per-bit to noise power spectral density ratio (E_b/N_0) with the measured PER. The symbol error rate for DQPSK systems as a function of E_b/N_0 is derived in [36]. From this function, the ideal PER curve in Fig. 13 was found by injecting uniformly distributed symbol errors into 10^6 symbols taken from the GNU radio FIFO (Fig. 11), decoding these symbols, and then calculating the PER. The measured PER was found by transmitting 10^6 backscatter DQPSK symbols at 25 Mbps in a cabled setup with an attenuator in series. As the channel attenuation was increased, the backscattered signal power was measured using an Agilent N9010A spectrum analyzer, and values of E_b/N_0 were calculated using the 5 dB noise figure of the
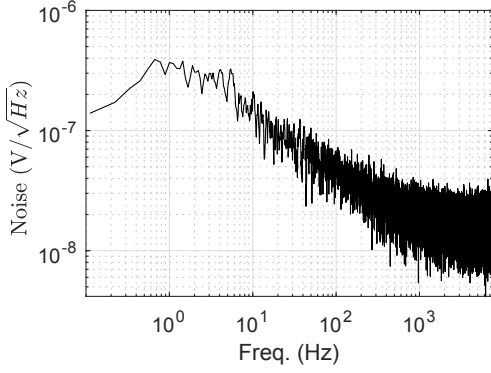
Fig. 14. Measured input-referred noise spectral density of the NeuroDisc's biosignal front-end

Analog Devices low-noise amplifier within the USRP [35]. The symbols received at the USRP were then decoded in the receiver pipeline shown in Fig. 11. It can be observed that the receiver performs 12 dB worse than the theory for a PER of 0.1%. This discrepancy in performance is likely due to non-idealities in the demodulation process, including non-ideal symbol frequency synchronization, leaked carrier power, and constellation skew.

C. Error Vector Magnitude Measurement

The NeuroDisc's DQPSK backscatter constellation was evaluated by measuring the error vector magnitude (EVM) at the receiver. The EVM is a figure of merit for how well the measured constellation points align with the ideal DQPSK constellation points [37]:

$$\text{EVM} = 100 \cdot \sqrt{\frac{\frac{1}{N}\sum_{k=1}^{N}|\hat{S}_{k_{ideal}} - S_{k_{sample}}|^2}{\frac{1}{N}\sum_{k=1}^{N}|\hat{S}_{k_{ideal}}|}}, \qquad (4)$$

where N is the total number of symbols transmitted, $S_{k_{sample}}$ is the normalized k-th demodulated symbol location in the I/Q plane, and $\hat{S}_{k_{ideal}}$ is the ideal normalized symbol position. To measure EVM, the NeuroDisc transmitted five thousand packets, translating to $> 5 \times 10^6$ bits. The EVM was calculated to be 9.69 % for the measured constellation shown in Fig. 9(b).

D. Characterization of Noise in the Biosignal Interface

Interference is a major concern with wireless neural recorders because sensitive biosignal interfaces are in close physical proximity to high-energy RF and digital signals. To address the risk of signal interference on the circuit board, we measured the input-referenced noise on NeuroDisc's biosignal amplifier. All sixteen measurement channels were grounded and the Comms FPGA was configured to operate nominally, as described in Section II. The NeuroDisc was placed in a Faraday cage to reduce 60 Hz interference from the mains power, and it was connected to the receiver via a UMC-to-SMA cable in order to uplink the data from inside the cage. The NeuroDisc's biosignal front-end was configured with a
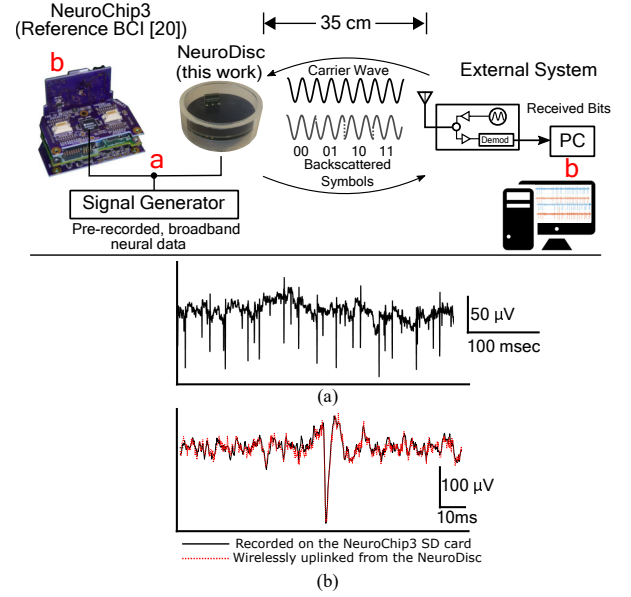

Fig. 15. Performance of the NeuroDisc with the 25 Mbps backscatter uplink was compared to a reference BCI, the NeuroChip3 [22]. (a) Pre-recorded neural data containing LFP and neural spikes was output from a signal generator and measured by both BCIs. (b) Reconstructed data at the NeuroDisc's external system shows good agreement with samples recorded on the NeuroChip3's SD card.

20 kHz sampling rate and with a band-pass filter having cutoff frequencies of 1.6 Hz – 7.5 kHz. Ten seconds' worth of samples were collected. Analyzing the received data at the receiver, the measured input-referenced noise was found to be 2.35 µVrms, which shows good agreement with the 2.4 µVrms noise specified in the Intan RHS2116 datasheet, and further shows that the NeuroDisc RF and digital systems do not add significant noise to sensitive biosignal measurements. The measured noise power spectral density from this measurement is shown in Fig. 14.

E. Signal Chain Validation with Pre-Recorded Data

Once the backscatter uplink and biosignal interface had been characterized and shown to be functional, the complete signal chain of the NeuroDisc was validated, as shown in Fig 15. Pre-recorded broadband neural data with an amplitude <900 µV (Fig. 15(a)) was output from an Agilent 33500B arbitrary waveform generator and measured by the NeuroDisc (this work) as well as a reference BCI system (University of Washington Neurochip-3, a recent revision of the NeuroChip2 [7], [22]). The NeuroDisc wirelessly transferred data to the External System using the 25 Mbps backscatter uplink at a distance of 0.35 m, while the NeuroChip3 saved the recorded data to an on-board SD card. Both the NeuroDisc and the NeuroChip3 were configured to sample at 20 kHz while using a 1 Hz – 7.5 kHz band-pass filter and a 1.6 Hz digital high-pass filter. The data received from the NeuroDisc was then plotted over the data recorded by the NeuroChip3 as shown in Fig. 15(b) showing good agreement.

TABLE II
COMPARISON OF STATE-OF-THE-ART WIRELESS NEURAL RECORDERS

	Yin et al., 2014 [8]	*Schwarz et al., 2014 [9]*	*Muller et al., 2015 [18]*	*Ando et al., 2016 [38]*	*Teng et al., 2017 [39]*	*Xu et al., 2018 [40]*	*This Work*
Test Subject	NHP	NHP	Rat	Humans	_ᵃ	Rat	**NHP**
BCI Size (mm)	52 x 44 x 30	_ᵃ	6.4 x 6.4 x 0.7 (IC)	53 x 31 x 47 (Transmitter)	1 x 1 (IC)	2.5 x 5.3 (IC)	**63 x 63 x 30**
ADC (bits)	12	12	15	12	_ᵃ	12	**16**
No. of Channels	100	512	64	4096	8	12	**16**
Sampling (kSps)	20	31	1	1	_ᵃ	40	**20**
RF Comms Type	Active RF	Active RF	ASK Backscatter	Active RF	Active RF	Active RF	**DQPSK Backscatter**
RF Comms Band	3.5 GHz	2.4 GHz	300 MHz	9 GHz	403 MHz	2.4 GHz	**909 MHz**
Wireless Data Rate (Mbps)	48	1.33	1	128	8	10	**25**
Uplink Distance (m)	5	10	0.013	5	_ᵃ	_ᵃ	**0.35ᶜ**
Analog Comms Power (mW)	>30ᵃ	33.9ᵇ	0.0024	561	5.6	396	**0.309ᵈ**
Analog Comms Energy Efficiency (pJ/bit)	>180 (high-rate mode) - 750 (low rate mode)ᵃ	25,488	2.4	4383	700	39,600	**12.4**

ᵃExact value not reported. ᵇTX power consumption of the nRF24L01+ at 0 dBm transmit power.
ᶜFree-space distance for *in vivo* measurements. ᵈMeasured static+dynamic power of the backscatter modulator.
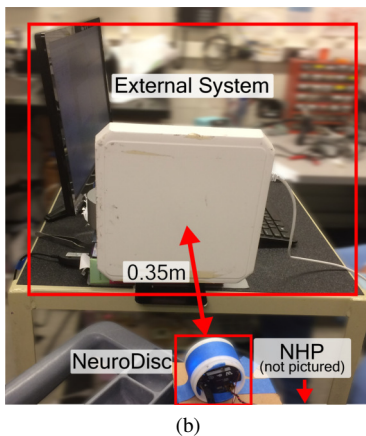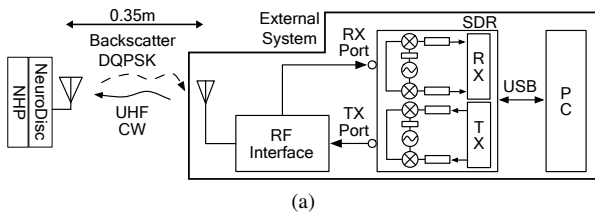

(a)

(b)

Fig. 16. Recordings were performed by connecting the NeuroDisc's biosignal front-end to an *in vivo* micro-electrode array previously implanted in the primary motor cortex of a pigtail macaque. (a) Block diagram and (b) photo of the *in vivo* experimental setup (NHP not pictured due to site policy).

F. Validation with in vivo microelectrode array

Measurements were performed with an *in vivo* micro-electrode array to validate the NeuroDisc's biosignal interface and high-rate wireless backscatter uplink. Neural signals were recorded from an anesthetized pigtail macaque (*Macaca nemestrina*) who had a 96-channel Utah Array (Blackrock Microsystems) chronically implanted in the primary motor cortex (M1). The experiments were performed at the Washington National Primate Research Center in Seattle, WA, USA, and all experimental procedures were approved by the University of Washington (UW) Institutional Animal Care and Use Committee. Support was provided by personnel from the UW Department of Physiology and Biophysics.

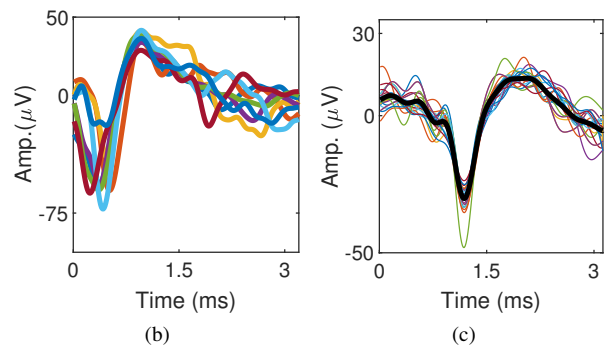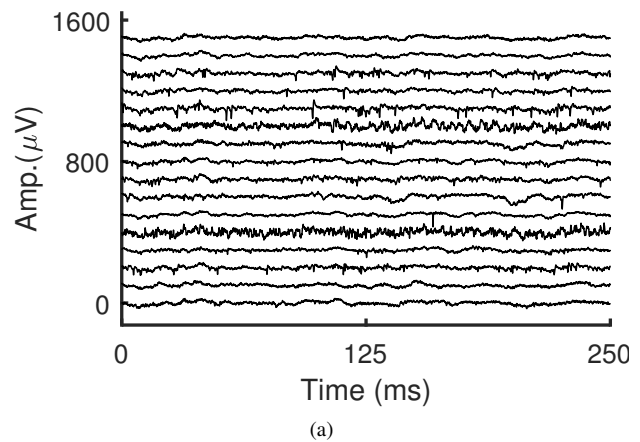The NHP and the NeuroDisc were on a plastic surgical

(a)

(b)

(c)

Fig. 17. *In vivo* data was uplinked to the External System. (a) Time series plot of all 16 channels of measured neural data. Offline spike sorting was then performed on the data based on [41] (b) Plot of five mean spike waveforms identified in one channel of the data. (c) Plot of the spikes identified within one cluster overlayed with the mean waveform.

table that had clear line-of-sight to the External System antenna on a cart 0.35 m away, as shown in Fig. 16. All 16 recording channels of the NeuroDisc were connected to the monkey's implanted electrode via a 17 cm shielded cable. The NeuroDisc was pre-configured to record from all sixteen channels with a sampling rate of 20 kSps with 16-bit resolution per channel. The biosignal front-end was configured with a 1 Hz – 7.5 kHz band-pass filter and a 1.6 Hz digital high-pass filter to remove low-frequency offsets from the data.

Neural signals recorded by the NeuroDisc were uplinked

to the External System using the 25 Mbps wireless backscatter uplink. The data was decoded and plotted offline using Matlab. A time-series plot of all sixteen channels is shown in Fig. 17(a). Low frequency fluctuations corresponding to local field potentials (LFPs) as well as higher frequency neural spikes can be observed in the data. Some channels exhibited higher noise (e.g. the fifth channel from the bottom in Fig. 17(a)) that could be attributed to neural cell loss or glial scarring due to the chronically implanted micro-electrode array. To validate that the neural recordings captured biologically relevant signals, spike detection and classification using an unsupervised k-means classifier were applied to the data set using methods presented in [41]. Several neural spike families were identified in the data with examples from a single channel shown in Fig. 17(b) and (c).

IV. Conclusion & Future Work

In this work, we have introduced a 25 Mbps DQPSK wireless backscatter uplink for use with NeuroDisc brain-computer interface that demonstrates the viability of backscatter uplinks for wireless BCI applications. A comparison of state-of-the-art neural recorders including the NeuroDisc is shown in Table II. Compared to commercial radio uplinks such as Bluetooth Low Energy or 802.11n WiFi with communication efficiencies >4 nJ/bit, the NeuroDisc's DQPSK backscatter uplink is more efficient with a measured energy efficiency of 12.4 pJ/bit. The 25 Mbps data rate of the backscatter uplink represents a 4X improvement compared to previous work in [21]. These improvements were enabled by the design of a wideband UHF antenna, an FPGA-based digital data acquisition system with an integrated DQPSK modulator, and full-duplex DQPSK backscatter receiver providing an average isolation of 89 dB. The system's complete signal chain was validated using pre-recorded neural data and *in vivo* neural recordings from a pigtail macaque.

Future work will focus on maturing the NeuroDisc and its backscatter uplink system for experiments on awake, freely moving monkeys. The NeuroDisc's analog communication efficiency and overall power consumption could be improved by developing a custom integrated circuit with an inductor-free DQPSK modulator based on the digital design demonstrated in this work and the approach of [27]. The range of the system could be improved by exploring new antenna designs with more favorable gain and gain patterns, as well as by reducing parasitic losses in the self-jammer canceller. Lastly, a custom high-throughput backscatter receiver based on the design in this work could enable near-real time analysis of uplinked neural samples.

Acknowledgment

References

[1] E. V. Evarts, "Temporal patterns of discharge of pyramidal tract neurons during sleep and waking in the monkey," *Physiology*, vol. 27, no. 2, pp. 152–171, Mar. 1964.

[2] A. P. Georgopoulos, J. F. Kalaska, R. Caminiti, and J. T. Massey, "On the relations between the direction of two-dimensional arm movements and cell discharge in primate motor cortex," *J. Neuroscience*, vol. 2, no. 11, pp. 1527–1537, 1982.

[3] A. L. Orsborn *et al.*, "Closed-loop decoder adaptation shapes neural plasticity for skillful neuroprosthetic control," *Neuron*, vol. 82, no. 6, pp. 1380 – 1393, 2014.

[4] L. R. Hochberg *et al.*, "Reach and grasp by people with tetraplegia using a neurally controlled robotic arm," *Nature*, vol. 485, pp. 372–375, May 2012.

[5] J. L. Collinger *et al.*, "High-performance neuroprosthetic control by an individual with tetraplegia," *The Lancet*, vol. 381, no. 9866, pp. 557–564, 2013.

[6] A. Jackson, J. Mavoori, and E. E. Fetz, "Correlations between the same motor cortex cells and arm muscles during a trained task, free behavior, and natural sleep in the macaque monkey," *Physiology*, vol. 97, no. 1, pp. 360–374, Jan. 2007.

[7] S. Zanos, A. G. Richardson, L. Shupe, F. P. Miles, and E. E. Fetz, "The Neurochip-2: an autonomous head-fixed computer for recording and stimulating in freely behaving monkeys," *IEEE Trans. Neural Syst. Rehabil. Eng.*, vol. 19, no. 4, pp. 427–435, 2011.

[8] M. Yin *et al.*, "Wireless neurosensor for full-spectrum electrophysiology recordings during free behavior," *Neuron*, vol. 84, no. 6, pp. 1170–1182, Dec 2014.

[9] D. A. Schwarz *et al.*, "Chronic, wireless recordings of large-scale brain activity in freely moving rhesus monkeys," *Nature Methods*, vol. 11, no. 6, p. 670, 2014.

[10] J. Rosenthal and M. S. Reynolds, "A 158 pJ/bit 1.0 Mbps bluetooth low energy (BLE) compatible backscatter communication system for wireless sensing," in *2019 IEEE Topical Conference on Wireless Sensors and Sensor Networks (WiSNet)*, Jan 2019.

[11] J. F. Ensworth and M. S. Reynolds, "Every smart phone is a backscatter reader: Modulated backscatter compatibility with Bluetooth 4.0 Low Energy (BLE) devices," in *Proc. 2015 IEEE Intl. Conf. RFID (RFID 15)*, 2015.

[12] X. Liu *et al.*, "Design of a closed-loop, bidirectional brain machine interface system with energy efficient neural feature extraction and PID control," *IEEE Trans. Biomed. Circuits Syst.*, vol. 11, no. 4, pp. 729–742, Aug 2017.

[13] J. A. Fernandez-Leon *et al.*, "A wireless transmission neural interface system for unconstrained non-human primates," *J. Neural Eng*, vol. 12, no. 5, p. 056005, Oct 2015.

[14] H. Stockman, "Communication by means of reflected power," *Proceedings of the IRE*, vol. 36, no. 10, pp. 1196–1204, Oct 1948.

[15] S. J. Thomas, R. R. Harrison, A. Leonardo, and M. S. Reynolds, "A battery-free multichannel digital neural/EMG telemetry system for flying insects," *IEEE Trans. Biomed. Circuits Syst.*, vol. 6, no. 5, pp. 424–436, Oct 2012.

[16] J. D. Griffin and G. D. Durgin, "Complete link budgets for backscatter-radio and RFID systems," *IEEE Antennas and Propagation Magazine*, vol. 51, no. 2, pp. 11–25, April 2009.

[17] A. Sharma, E. Kampianakis, J. Rosenthal, A. Pike, A. Dadkhah, and M. S. Reynolds, "Wideband UHF DQPSK backscatter communication in reverberant cavity animal cage environments," *IEEE Trans. Antennas Propag.*, pp. 1–1, 2019.

[18] R. Muller *et al.*, "A minimally invasive 64-channel wireless μECoG implant," *IEEE J. Solid-State Circuits*, vol. 50, no. 1, pp. 344–359, 2015.

[19] S. J. Thomas and M. S. Reynolds, "A 96 Mbit/sec, 15.5 pJ/bit 16-QAM modulator for UHF backscatter communication," in *Proc. 2012 IEEE Intl. Conf. RFID (RFID 12)*, Apr. 2012, pp. 185–190.

[20] A. Shirane, H. Tan, Y. Fang, T. Ibe, H. Ito, N. Ishihara, and K. Masu, "A 5.8 GHz RF-powered transceiver with a 113 μw 32-QAM transmitter employing the IF-based quadrature backscattering technique," in *2015 IEEE Intl. Solid-State Circuits Conf.- (ISSCC) Digest of Technical Papers*, Feb 2015, pp. 1–3.

[21] J. Rosenthal, E. Kampianakis, A. Sharma, and M. S. Reynolds, "A 6.25 Mbps, 12.4 pJ/bit DQPSK backscatter wireless uplink for the NeuroDisc brain-computer interface," in *Proc. 2018 IEEE Biomed. Circuits Syst. Conf. (BioCAS)*, Oct 2018.

[22] NeuroChip3. [Online]. Available: depts.washington.edu/fetzweb/neurochip3.html

[23] CST Microwave Studio. [Online]. Available: cst.com/products/cstmws

[24] Intan Technologies, LLC. RHS2000 series digital stimulator and amplifier chips. [Online]. Available: http://intantech.com/

[25] Intel MAX10 FPGA. [Online]. Available: intel.com/content/www/us/en/products/programmable.html

[26] R. W. Hamming, "Error detecting and error correcting codes," *The Bell System Technical Journal*, vol. 29, no. 2, pp. 147–160, April 1950.

[27] S. J. Thomas, E. Wheeler, J. Teizer, and M. S. Reynolds, "Quadrature amplitude modulated backscatter in passive and semipassive UHF RFID systems," *IEEE Trans. Microwave Theory Tech.*, vol. 60, no. 4, pp. 1175–1182, April 2012.

[28] R. Correia, A. Boaventura, and N. B. Carvalho, "Quadrature amplitude backscatter modulator for passive wireless sensors in IoT applications," *IEEE Trans. Microw. Theory Techn.*, vol. 65, no. 4, pp. 1103–1110, April 2017.

[29] J. Kimionis and M. M. Tentzeris, "Pulse shaping: The missing piece of backscatter radio and RFID," *IEEE Trans. Microw. Theory Techn.*, vol. 64, no. 12, pp. 4774–4788, Dec 2016.

[30] A. Dadkhah, J. Rosenthal, and M. S. Reynolds, "ZeroScatter: Zero-added-component backscatter communication using existing digital I/O pins," in *Proc. 2019 IEEE Topical Conf. on Wireless Sensors and Sensor Networks (WiSNet)*, Jan 2019.

[31] K. Kurokawa, "Power waves and the scattering matrix," *IEEE Trans. Microw. Theory Techn.*, vol. 13, no. 2, pp. 194–202, March 1965.

[32] P. V. Nikitin, K. V. S. Rao, and R. D. Martinez, "Differential RCS of RFID tag," *Electronics Letters*, vol. 43, no. 8, pp. 431–432, 2007.

[33] D. M. Dobkin, *The RF in RFID: Passive UHF RFID in Practice*. Newnes (Elsevier), 2008.

[34] A. Boaventura, J. Santos, A. Oliveira, and N. B. Carvalho, "Perfect isolation: dealing with self-jamming in passive RFID systems," *IEEE Microwave Magazine*, vol. 17, no. 11, pp. 20–39, Nov 2016.

[35] Analog devices . AD9364 Noise Figure vs. Gain Index Plots. [Online]. Available: https://ez.analog.com/wide-band-rf-transceivers/design-support/w/documents/10073/noise-figure-vs-gain-index-plots

[36] J. G. Proakis and M. Salehi, *Fundamentals of Communication Systems–2nd Ed.* Essex: Pearson, 2014.

[37] S. Thomas and M. S. Reynolds, "QAM backscatter for passive UHF RFID tags," in *Proc. 2010 IEEE Intl. Conf. RFID (RFID 10)*, April 2010, pp. 210–214.

[38] H. Ando, K. Takizawa, T. Yoshida, K. Matsushita, M. Hirata, and T. Suzuki, "Wireless multichannel neural recording with a 128-Mbps UWB transmitter for an implantable brain-machine interfaces," *IEEE Trans. Biomed. Circuits Syst.*, vol. 10, no. 6, pp. 1068–1078, Dec 2016.

[39] K. Teng, T. Wu, X. Liu, Z. Yang, and C. Heng, "A 400 MHz wireless neural signal processing IC with 625 × on-chip data reduction and reconfigurable BFSK/QPSK transmitter based on sequential injection locking," *IEEE Trans. Biomed. Circuits Syst.*, vol. 11, no. 3, pp. 547–557, June 2017.

[40] J. Xu, A. T. Nguyen, W. Zhao, H. Guo, T. Wu, H. Wiggins, E. W. Keefer, H. Lim, and Z. Yang, "A low-noise, wireless, frequency-shaping neural recorder," *IEEE Trans. Emerg. Sel. Topics Circuits Syst."*, vol. 8, no. 2, pp. 187–200, June 2018.

[41] F. J. Chaure, H. G. Rey, and R. Quian Quiroga, "A novel and fully automatic spike-sorting implementation with variable number of features," *J. Neurophysiology*, vol. 120, no. 4, pp. 1859–1871, 2018.

Apoorva Sharma (S'15) received the B.Tech degree in electronics and communication engineering from Galgotias College of Engineering and Technology (GCET), India, in 2009 and M.Sc (tech) degree from International Institute of Information Technology Hyderabad, India (IIIT-H) in 2011.

From 2011 to 2013 she was with Computer Simulation Technology India, where she held the position of Application Engineer and was responsible for technical support and benchmarks for CST Microwave Studio, Cable Studio, Particle Studio and Design Studio software. She also helped in improving the database of Antenna Magus. Since July 2015 she is with the Department of Electrical Engineering at University of Washington, Seattle, WA, USA as a Ph.D student. Her research interests include modeling and optimization techniques of RF devices, electromagnetics, antenna designs and implantable devices.

Eleftherios Kampianakis (S'15) received the B.S. and M.S. in Electronic and Computer Engineering from the Technical University of Crete, Greece. His diploma thesis on over-the-air programmable wireless sensor networks (WSN) received best diploma thesis award on the pan-hellenic IEEE VTS & AESS Joint Greece Chapter Final/Diploma Thesis Competition for the years 2009-2011. During his M.S. he developed a low-cost and low-power WSN for environmental sensing exploiting backscatter communication principles. His contribution has been selected as one of the best papers at the IEEE SENSORS Conference 2013.

He is currently working on his Ph.D in the Department of Electrical Engineering at the University of Washington, Seattle, WA, USA. His research interests include backscatter communication and implantable biomedical devices.

Matthew S. Reynolds (S'01–M'02–SM'10) received the S.B., M.Eng., and Ph.D. degrees from the Massachusetts Institute of Technology (MIT), Cambridge, MA, USA, in 1998, 1999, and 2003, respectively.

He is currently an Associate Professor of Electrical Engineering and Computer Science and Engineering at the University of Washington, Seattle, WA, USA. He is a co-founder of the RFID systems firm, ThingMagic Inc., the demand-side energy conservation technology firm Zensi, the home sensing company SNUPI Inc, and the millimeter wave imaging firm ThruWave LLC. His research interests include the physics of sensors and actuators, RF identification (RFID), microwave and millimeter wave imaging, and sensor signal processing.

James Rosenthal (S'16) received the B.S. degree in Electrical Engineering from the University of Minnesota, Minneapolis, MN, USA in 2013 and the M.S. degree in Electrical Engineering from the University of Washington in 2018.

From 2013 to 2016 he was an electrical engineer at NASA Langley Research Center where he designed avionics systems for aerospace research projects. Since 2016 he has been a Ph.D. student in the Department of Electrical & Computer Engineering at University of Washington in Seattle, WA, USA. His research is focused on the design of ultra-low power backscatter communication systems for biomedical applications.